RAPID COMMUNICATIONS

PHYSICAL REVIEW B **93**, 201101(R) (2016)

$TaIrTe_4$: A ternary type-II Weyl semimetal

K. Koepernik,[1] D. Kasinathan,[2] D. V. Efremov,[1] Seunghyun Khim,[1] Sergey Borisenko,[1] Bernd Büchner,[1,3]
and Jeroen van den Brink[1,3,4]
[1]*IFW Dresden, P.O. Box 270116, 01171 Dresden, Germany*
[2]*Max-Planck-Institut für Chemische Physik fester Stoffe, Nöthnitzer Strasse 40, 01187 Dresden, Germany*
[3]*Department of Physics, TU Dresden, 01062 Dresden, Germany*
[4]*Department of Physics, Harvard University, Cambridge, Massachusetts 02138, USA*
(Received 14 March 2016; revised manuscript received 20 April 2016; published 5 May 2016)

In metallic condensed matter systems two different types of Weyl fermions can in principle emerge, with either a vanishing (type-I) or with a finite (type-II) density of states at the Weyl node energy. So far only WTe_2 and $MoTe_2$ were predicted to be type-II Weyl semimetals. Here we identify $TaIrTe_4$ as a third member of this family of topological semimetals. $TaIrTe_4$ has the attractive feature that it hosts only four well-separated Weyl points, the minimum imposed by symmetry. Moreover, the resulting topological surface states—Fermi arcs connecting Weyl nodes of opposite chirality—extend to about 1/3 of the surface Brillouin zone. This large momentum-space separation is very favorable for detecting the Fermi arcs spectroscopically and in transport experiments.

DOI: 10.1103/PhysRevB.93.201101

Weyl fermions are massless chiral fermions with a fundamental role in quantum field theory and high-energy physics [1]. In low-energy condensed matter systems Weyl fermions can emerge as quasiparticles: in semimetals with either broken time-reversal symmetry or inversion symmetry, they can appear at the crossing point of two linearly dispersing three-dimensional bands [2–4]. These Weyl nodes and their chirality are protected by the symmetry of the semimetal and the topology of its electronic band structure. As a consequence Weyl semimetals (WSMs) host topologically protected surface states in the form of open arcs—Fermi arcs—terminating at the projection of bulk Weyl points (WPs) of opposite chirality. Other physical consequences in WSMs are exotic transport phenomena such as a large negative magnetoresistance with unusual anisotropy [5].

Very recently it was pointed out that whereas in high-energy physics there is only one kind of Weyl fermion, in condensed matter systems there are two, and not more than two, types of WPs [6]. In a type-I WSM the bulk Fermi surface shrinks to a point at the Weyl node, whereas in a type-II WSM the Weyl cone arises as a connector of hole and electron pockets, where the large tilt of the cone induces a finite density of states at the node energy. This fundamental difference can, for instance, cause an anomalous Hall effect in type-II WSMs [6–8]. The type-I Weyl fermion is similar to the one also encountered in high-energy physics. In type-II systems, however, the Weyl nodes appear at touching points between electron and hole pockets so that the WP arising in this low-energy condensed matter setting [9,10] lacks a high-energy equivalent.

A number of type-I WSMs have been predicted theoretically [2,3,11–13]. The first experimental indication for the presence of Weyl points and Fermi arcs has been established in a class of TaAs related compounds [14–22] using angle-resolved photoemission spectroscopy (ARPES)—even if the large number of WPs (24) makes the interpretation of spectroscopic and transport data quite complicated in these TaAs-based systems. Type-II WSMs are very sparse at the moment—this category has barely been explored and only two potential materials, orthorhombic WTe_2 and $MoTe_2$, have been identified theoretically [6,23,24]. Here we identify the orthorhombic ternary compound $TaIrTe_4$ as a third type-II WSM. Based on calculations of its electronic structure and topological properties, we predict that $TaIrTe_4$ hosts only four type-II WPs, the minimal number of WPs a system with time-reversal invariance can host [24]. The WPs are very well separated from each other in momentum space: topological Fermi arcs that connect WPs of opposite chirality extend to about 1/3 of the surface Brillouin zone, and are present on both inequivalent surface terminations. Such a large momentum-space separation is conducive to easy detection of the Fermi arcs in spectroscopy experiments as well as to resolve their contribution to transport.

We performed density functional theory (DFT) calculations within the local density approximation [25] using the full-potential local-orbital (FPLO) code [26]. For the Brillouin zone (BZ) integration we used the tetrahedron method with a $12\times6\times6$ **k**-mesh. Scalar relativistic calculations [without spin-orbit coupling (SOC)] and full four-component relativistic calculations (including SOC) were performed. For easier analysis, a model has been extracted using maximally projected Wannier functions (WFs) for the Ta $5d$, Ir $5d$, and Te $5p$ orbitals. The resulting (high accuracy) model reproduces the band energies of all occupied bands and unoccupied bands up to 1 eV above the Fermi level accurately. For faster evaluation of all subsequent calculations the real space extent of the WFs has been reduced resulting in a model which shows some deviations of up to 10 meV around and slightly below the Fermi level, especially off the $k_z = 0$ plane. These deviations of the reduced model slightly change the Fermi surface (FS) especially for $E = 0$ eV but not in the important BZ region. We have checked that all topological properties are present in the accurate WF model as well.

$TaIrTe_4$ crystallizes in a noncentrosymmetric orthorhombic structure with space group 31 ($Pmn2_1$) [27]. The lattice constants are $a = 3.77$ Å, $b = 12.421$ Å, and $c = 13.184$ Å. The unit cell contains four formula units which form two layers of distorted corner sharing octahedra. This compound has the same space group as $MoTe_2$ and WTe_2 but in contrast to those,

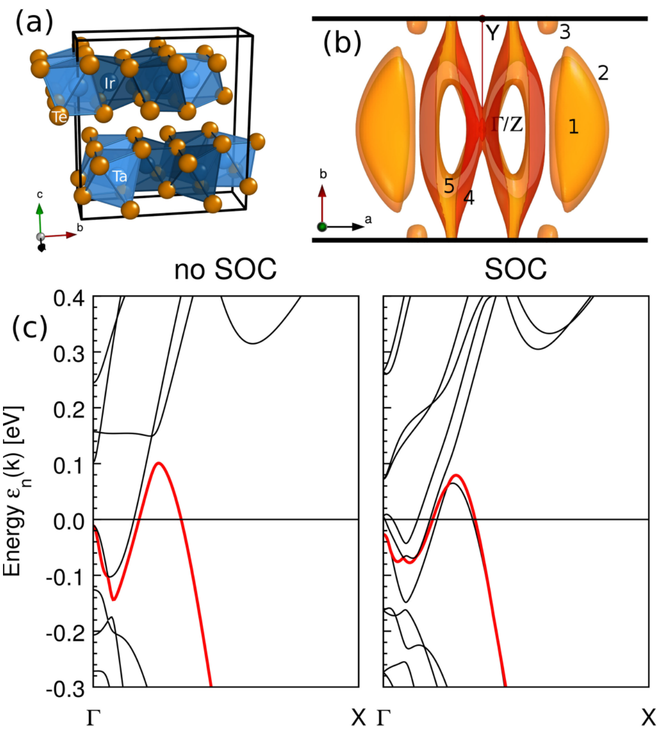

FIG. 1. (a) Crystal structure, (b) Fermi surface of the accurate WF model, and (c) band structure along the line ΓX both without and with SOC. Only the part of the BZ containing Fermi surfaces is shown in panel (b).

the size of the unit cell is doubled in the b direction [Fig. 1(a)]. A detailed list of the Wyckoff positions can be found in the Supplemental Materials [28].

Although sharing the same space group with the binary tellurides, the similarities of the $TaIrTe_4$ band structure compared to $MoTe_2$ and WTe_2 should not be overemphasized, since the Fermi surfaces are quite different. Figure 1(c) shows the band structure along the line ΓX without and with SOC. The band shown in red forms the top of the valence band. It gives rise to three-dimensional hole pockets along the line ΓX. Upon inclusion of SOC, all bands split almost everywhere, which leads to two nested but not touching hole pockets [Fig. 1(b), labeled 1 and 2]. The conduction bands around the Γ point form two electron pockets (labeled 4 and 5) which exhibit a noticeable two-dimensional character in the k_z direction in contrast to the hole pockets. In contrast to $MoTe_2$ and WTe_2, the hole and electron character of the pockets are interchanged in $TaIrTe_4$. Note that pockets 4 and 5 have open Fermi surfaces across the $k_y = \pm\pi$ BZ boundaries for $k_z = \pm\pi$. This feature is absent in the reduced WF model at $E = 0$ eV but reemerges 8 meV above the Fermi level. Additionally, small hole pockets [Fig. 1(b), label 3] occur at the $k_y = \pm\pi$ planes. Another notable difference to $MoTe_2$ and WTe_2 is the fact that the top of the valence band crosses the bottom of the conduction band close to the Γ point along the line ΓX in $TaIrTe_4$.

Despite the difference in the hole/electron nature of the pockets, $TaIrTe_4$ has similarities in its topological properties compared to the two binary tellurides. Due to symmetry conditions Weyl points can only occur in the $k_z = 0$ plane [6,24]. Without SOC we find eight (spinless) Weyl points between the topmost valence band N and the lowest conduction band $N+1$. Each quadrant of the k_x, k_y plane contains two such points with opposite Chern number C. The one with negative chirality (WP1) resides in the hole pocket around $k_x = 0.1178$, while the one with positive chirality (WP2) resides in the electron pocket around $k_x = 0.0483$ (see Table I and Fig. 2).

TABLE I. Positions, Chern numbers, and energies of the Weyl points formed by the topmost valence band N and the lowest conduction band $N+1$.

	Band N	SOC	Position in $(\frac{2\pi}{a}, \frac{2\pi}{b}, \frac{2\pi}{c})$	C	E (meV)
WP1	60	No	(0.1178, 0.1529, 0)	−1	115
WP2	60	No	(0.0483, 0.2306, 0)	+1	−79
WP	120	Yes	(0.1237, 0.1627, 0)	−1	82.7

With SOC, the spin doubled Weyl points get split and moved around and due to the strength of the SOC, pairs of WP2 with opposite chirality are annihilated in the process. Of the spin doubled Weyl points WP1 only a single point (WP) survives per quadrant which results in a total of four Weyl points in the BZ if SOC is included. Two WPs with opposite chirality sit in the hole pocket around $k_x = 0.1237$ resulting in a zero Chern number for the hole pocket. It is interesting to note that WP1 and WP2 (without SOC) are type-I Weyl points (see Supplemental Material) while WP (with SOC) is type II.

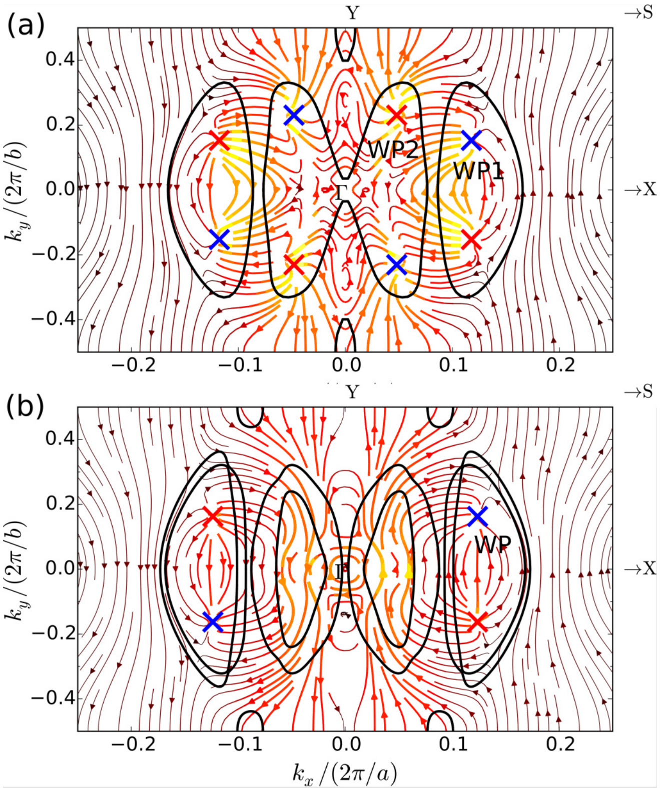

FIG. 2. The flux of the k_z-averaged Berry curvature in the k_x, k_y plane (a) without and (b) with SOC. Crosses mark the Weyl points (blue $C = -1$, red $C = +1$). The black solid curves are $k_z = 0$ cuts through the bulk Fermi surface at $E = 0$ eV.

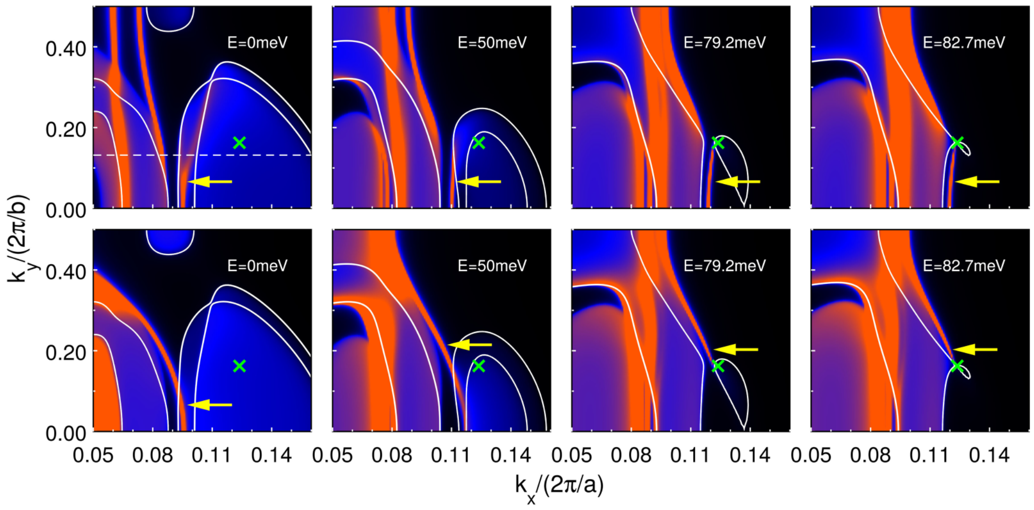

FIG. 3. Surface Fermi surface with SOC of (upper row) the (001) surface and (lower row) the $(00\bar{1})$ surface for various energies. The position of the WP is marked with a cross. The emergence of the Fermi arcs are marked by the arrows. The solid lines are $k_z = 0$ cuts of the $E = 0$ bulk Fermi surface.

In order to establish the topology of the electronic structure, we implemented the calculation of the Berry curvature $\mathbf{F}(\mathbf{k}) = \nabla_{\mathbf{k}} \times \mathbf{A}(\mathbf{k})$ with $\mathbf{A}(\mathbf{k}) = -i\langle u_{\mathbf{k}} \mid \nabla_{\mathbf{k}} u_{\mathbf{k}}\rangle$ into FPLO following the method of Ref. [29]. From this we calculated the Chern number $C = \frac{1}{2\pi}\oint_s \mathbf{F} \cdot d\mathbf{S}$ as the flux of the Berry curvature of all bands up to and including band N through a closed surface surrounding the Weyl point. Here, we applied the technique of choosing a small sphere around the WP such that bands N and $N + 1$ are separated by a gap all over the sphere [6,24]. The results are summarized in Table I.

For illustration, the Berry curvature of the N lowest bands was calculated over the whole BZ followed by an integration over k_z which results in the averaged Berry curvature projected onto the k_x,k_y plane. The resulting flux picture is shown in Fig. 2 without SOC (a) and with SOC (b). (Note that only half the extent of the BZ in k_x-direction is shown.) With the sign choice of the Berry connection, the sinks of the flux have $C = -1$ and flux sources have $C = 1$. The monopoles at the Weyl points are clearly visible and lay well within the $k_z = 0$ cuts of the $E = 0$ bulk FS (solid lines). It is also obvious that there are no other Weyl points between bands N and $N + 1$.

There certainly are additional topological features in the band structure such as line nodes on the k_x,k_z plane as well as Weyl points between different sets of bands. We will not discuss them in this work mainly due to the fact that they will either be at energies further away from the Fermi energy or fall into the bulk band projections.

The Weyl points identified above give rise to topologically protected surface states. In our case the projection of the Weyl points onto the (001) direction, map single distinct WPs onto points in the surface BZ, in which case topologically protected Fermi arcs are to be expected [6]. Figure 3 shows the (001)-surface Fermi surface (spectral function) of an ideal semi-infinite slab. The spectral function was obtained via Green's function recursion [30,31] by mapping the bulk WF Hamiltonian onto the slab geometry while neglecting any surface and relaxation induced modifications to the Hamiltonian. Only part of the surface BZ is shown to focus on the essential details. Depicted is the spectral density of the first unit cell at the surface, i.e., the two topmost octahedral layers. For orientation, the Weyl point is marked by a cross and $k_z = 0$ cuts of the $E = 0$ bulk FS are shown as solid lines.

A noncentrosymmetric compound has two distinct surfaces: (001) and $(00\bar{1})$. Any Fermi arc emerging from a WP must be accompanied by another different arc living on the opposite surface. We choose two such surfaces by choosing the natural cleavage plane between the octahedral layers followed by a removal of either the upper or lower semi-infinite half of the bulk. The upper and lower panels of Fig. 3 show the evolution of the spectral function of the (001) and $(00\bar{1})$ surface, respectively, while increasing the energy from the bulk Fermi level at 0 meV to the WP energy 82.7 meV. At 0 meV the spectral function of the (001) surface shows the two hole pockets 1 and 2 (Fig. 1), containing the WP, as well as the hole pocket 3 and electron pockets 4 and 5 (around $k_x = 0.05$). Additionally, two trivial SO-split surface states (SSs) emerge out of the electron pockets running parallel to k_y at $k_x \approx 0.07$. The high intensity feature at the left side of the hole pockets marked by the arrow is the precursor of the Fermi arc, which will develop with increasing energy. At 0 meV, it is submerged into the bulk projected bands (BPBs). At 50 meV the electron pockets form open FSs along the k_y direction while the hole pockets shrink to such an extent that the Fermi arc is separated from the BPB forming a true SS. Yet, still the hole pockets are open across the $k_y = 0$ plane and contain two WPs with total Chern number zero, which opens the possibility of the arc being absorbed into the BPB due to perturbations. There is, however, no prohibition for an arc to be attached to a FS with zero total Chern number [32].

This changes at a critical energy ($E = 79.2$ meV) at which hole pocket 1 is collapsed and pocket 2 gets separated into two distinct closed pockets containing WPs of opposite chirality. At this stage the Fermi arc should be protected against perturbations. If the energy is raised to the WP energy, hole pocket 2 remains of finite size and has connected to the electron pocket at the coordinates of the Weyl point, which shows the

WP to be type II. Note how the Fermi arc is following the flux lines of the Berry curvature [Fig. 2(b)].

The lower row of Fig. 3 depicts the $(00\bar{1})$-surface FS for the same set of energies. The noticeable differences with respect to the other surface are the absence of the k_y-parallel SS and the emergence of the state connecting the hole pockets with the electron pockets marked by the arrow. This state evolves with increasing energy such that the point where it connects to the hole pocket moves closer to the WP, finally emerging exactly out of the Weyl point at WP energy. At $E = 79.2$ meV it can be best seen that this state is also a Fermi arc, only it does not connect two Weyl points in the same BZ as does the arc on the other surface. It rather connects two such points in adjacent BZs via immersion into the electron bulk states (see Supplemental Material for further elucidation.) At the WP energy it is not a freestanding arc anymore, due to it forming a surface resonance at the edge of the electron pocket. We checked that these arc features even survive the enormous perturbation introduced by cleaving the cell in the middle of the octahedral layer such that the surface is terminated by an unsaturated transition-metal layer. A slew of bond breaking related surface states appear in such a scenario. Yet the arcs remain, especially at energies between 50 and 82.7 meV.

To further elucidate the electronic structure of the Fermi arcs, we show the energy density cuts of the spectral density of the topmost unit cell of the semi-infinite slab for the (001)- and $(00\bar{1})$ surfaces along the line $\mathbf{k} = (\frac{2\pi}{a}k_x, \frac{2\pi}{b} \times 0.132, 0)$ in Fig. 4. The cut line is indicated by the dashed line in Fig. 3. The Fermi arc of the (001) surface is formed by a band which connects the top of the valence bands around $k_x = 0.07$ to the flank of the conduction band bottom around $k_x = 0.13$ as indicated by the arrows in the left panel of Fig. 4. The two intense bands in the electron pocket marked by circles are the two trivial SSs visible for $E = 0$ meV in the upper row of Fig. 3. The band forming the Fermi arc of the $(00\bar{1})$ surface connects the conduction band minimum around $k_x = 0.05$ to the top of the valence band of the hole pocket around $k_x = 0.12$. Hence, if superimposed in the same picture the two surface bands of the opposite surfaces represent two crossing bands bridging the gap as further illustrated in the Supplemental Material.

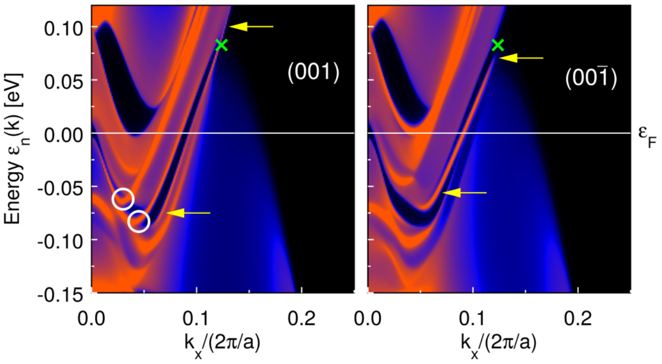

FIG. 4. Surface energy density cuts along the line $\mathbf{k} = (\frac{2\pi}{a}k_x, \frac{2\pi}{b} \times 0.132, 0)$ for the two surfaces.

In summary, we have demonstrated via DFT methods that the ternary compound TaIrTe$_4$ is a type-II Weyl semimetal with the simplest possible arrangement of Weyl points under the symmetry constraints of the compound. Topological Fermi arcs are present on both of the surfaces of a naturally cleaved ideal semi-infinite slab, as well as for other surface terminations. The length of the emerging Fermi arc of the (001) surface is about $1/3$ of the BZ extent in the b direction. The energy range in which the Fermi arcs should be detectable reaches from 50 to 82 meV above the Fermi level. All three telluride compounds show at least the minimum set of four Weyl points, occurring at very similar positions in k space. This seems to indicate that the existence of these particular Weyl points is a generic feature in this family of compounds, and it is therefore likely that slight modifications of the band filling (i.e., doping) can be used to bring the bulk Weyl points and the surface arcs connecting them at or even below the Fermi level where ARPES can resolve them.

K.K. is grateful to Hongbin Zhang for a valuable information exchange. D.K. acknowledges funding from the Deutsche Forschungsgemeinschaft (DFG) via FOR1346. This work was supported by the DFG through the Collaborative Research Center SFB 1143. J.vdB. acknowledges support from the Harvard-MIT CUA.

[1] H. Weyl, Z. Phys. **56**, 330 (1929).
[2] X. Wan, A. M. Turner, A. Vishwanath, and S. Y. Savrasov, Phys. Rev. B **83**, 205101 (2011).
[3] H. Weng, C. Fang, Z. Fang, B. A. Bernevig, and X. Dai, Phys. Rev. X **5**, 011029 (2015).
[4] L. Balents, Physics **4**, 36 (2011).
[5] D. T. Son and B. Z. Spivak, Phys. Rev. B **88**, 104412 (2013).
[6] A. A. Soluyanov, D. Gresch, Z. Wang, Q. Wu, M. Troyer, X. Dai, and B. A. Bernevig, Nature (London) **527**, 495 (2015).
[7] A. A. Zyuzin and R. P. Tiwari, arXiv:1601.00890.
[8] J. Ruan, S.-K. Jian, H. Yao, H. Zhang, S.-C. Zhang, and D. Xing, Nat. Commun. **7**, 11136 (2016).
[9] G. Volovik and M. Zubkov, Nucl. Phys. B **881**, 514 (2014).
[10] Y. Xu, F. Zhang, and C. Zhang, Phys. Rev. Lett. **115**, 265304 (2015).
[11] G. Xu, H. Weng, Z. Wang, X. Dai, and Z. Fang, Phys. Rev. Lett. **107**, 186806 (2011).
[12] A. A. Burkov and L. Balents, Phys. Rev. Lett. **107**, 127205 (2011).
[13] S. M. Huang, S. Y. Xu, I. Belopolski, C. C. Lee, G. Chang, B. Wang, N. Alidoust, G. Bian, M. Neupane, C. Zhang, S. Jia, A. Bansil, H. Lin, and M. Z. Hasan, Nat. Commun. **6**, 7373 (2015).
[14] S. Y. Xu, I. Belopolski, N. Alidoust, M. Neupane, G. Bian, C. Zhang, R. Sankar, G. Chang, Z. Yuan, C. C. Lee, S. M. Huang, H. Zheng, J. Ma, D. S. Sanchez, B. Wang, A. Bansil, F. Chou, P. P. Shibayev, H. Lin, S. Jia, and M. Z. Hasan, Science **349**, 613 (2015).

[15] L. X. Yang, Z. K. Liu, Y. Sun, H. Peng, H. F. Yang, T. Zhang, B. Zhou, Y. Zhang, Y. F. Guo, M. Rahn, D. Prabhakaran, Z. Hussain, S. K. Mo, C. Felser, B. Yan, and Y. L. Chen, Nat. Phys. **11**, 728 (2015).

[16] B. Q. Lv, H. M. Weng, B. B. Fu, X. P. Wang, H. Miao, J. Ma, P. Richard, X. C. Huang, L. X. Zhao, G. F. Chen, Z. Fang, X. Dai, T. Qian, and H. Ding, Phys. Rev. X **5**, 031013 (2015).

[17] S.-Y. Xu, I. Belopolski, D. S. Sanchez, C. Zhang, G. Chang, C. Guo, G. Bian, Z. Yuan, H. Lu, T.-R. Chang, P. P. Shibayev, M. L. Prokopovych, N. Alidoust, H. Zheng, C.-C. Lee, S.-M. Huang, R. Sankar, F. Chou, C.-H. Hsu, H.-T. Jeng, A. Bansil, T. Neupert, V. N. Strocov, H. Lin, S. Jia, and M. Z. Hasan, Sci. Adv. **1**, e1501092 (2015).

[18] X. Di-Fei, D. Yong-Ping, W. Zhen, L. Yu-Peng, N. Xiao-Hai, Y. Qi, D. Pavel, X. Zhu-An, W. Xian-Gang, and F. Dong-Lai, Chin. Phys. Lett. **32**, 107101 (2015).

[19] I. Belopolski, S.-Y. Xu, D. Sanchez, G. Chang, C. Guo, M. Neupane, H. Zheng, C.-C. Lee, S.-M. Huang, G. Bian, N. Alidoust, T.-R. Chang, B. Wang, X. Zhang, A. Bansil, H.-T. Jeng, H. Lin, S. Jia, and M. Z. Hasan, Phys. Rev. Lett. **116**, 066802 (2016).

[20] S. Souma, Z. Wang, H. Kotaka, T. Sato, K. Nakayama, Y. Tanaka, H. Kimizuka, T. Takahashi, K. Yamauchi, T. Oguchi, K. Segawa, and Y. Ando, Phys. Rev. B **93**, 161112(R) (2015).

[21] N. Xu, H. M. Weng, B. Q. Lv, C. E. Matt, J. Park, F. Bisti, V. N. Strocov, D. Gawryluk, E. Pomjakushina, K. Conder, N. C. Plumb, M. Radovic, G. Autès, O. V. Yazyev, Z. Fang, X. Dai, G. Aeppli, T. Qian, J. Mesot, H. Ding, and M. Shi, Nat. Commun. **7**, 11006 (2016).

[22] G. Chang, S.-Y. Xu, D. S. Sanchez, S.-M. Huang, C.-C. Lee, T.-R. Chang, H. Zheng, G. Bian, I. Belopolski, N. Alidoust, H.-T. Jeng, A. Bansil, H. Lin, and M. Zahid Hasan, arXiv:1512.08781.

[23] Y. Sun, S. C. Wu, M. N. Ali, C. Felser, and B. Yan, Phys. Rev. B **92**, 161107(R) (2015).

[24] Z. Wang, D. Gresch, A. A. Soluyanov, W. Xie, S. Kushwaha, X. Dai, M. Troyer, R. J. Cava, and B. A. Bernevig, arXiv:1511.07440.

[25] J. P. Perdew and Y. Wang, Phys. Rev. B **45**, 13244 (1992).

[26] K. Koepernik and H. Eschrig, Phys. Rev. B **59**, 1743 (1999), http://www.fplo.de.

[27] A. Mar, F. Jobic, and J. A. Ibers, J. Am. Chem. Soc. **114**, 8963 (1992).

[28] See Supplemental Material at http://link.aps.org/supplemental/10.1103/PhysRevB.93.201101 for structural data, Wannier model details and results of finite slab calculations.

[29] X. Wang, J. R. Yates, I. Souza, and D. Vanderbilt, Phys. Rev. B **74**, 195118 (2006).

[30] M. P. López-Sancho, J. M. López-Sancho, and J. Rubio, J. Phys. F: Met. Phys. **14**, 1205 (1984).

[31] M. P. López-Sancho, J. M. López-Sancho, and J. Rubio, J. Phys. F **15**, 851 (1985).

[32] F. D. M. Haldane, arXiv:1401.0529.